Indirect Assimilation of Radar Reflectivity with WRF 3D-Var and Its Impact on Prediction of Four Summertime Convective Events

HONGLI WANG AND JUANZHEN SUN

National Center for Atmospheric Research, Boulder, Colorado*

SHUIYONG FAN

Institute of Urban Meteorology, China Meteorological Administration, Beijing, China

XIANG-YU HUANG

National Center for Atmospheric Research, Boulder, Colorado*

(Manuscript received 28 April 2012, in final form 16 October 2012)

ABSTRACT

An indirect radar reflectivity assimilation scheme has been developed within the Weather Research and Forecasting model three-dimensional data assimilation system (WRF 3D-Var). This scheme, instead of assimilating radar reflectivity directly, assimilates retrieved rainwater and estimated in-cloud water vapor. An analysis is provided to show that the assimilation of the retrieved rainwater avoids the linearization error of the Z–q_r (reflectivity–rainwater) equation. A new observation operator is introduced to assimilate the estimated in-cloud water vapor. The performance of the scheme is demonstrated by assimilating reflectivity observations into the Rapid Update Cycle data assimilation and forecast system operating at Beijing Meteorology Bureau. Four heavy-rain-producing convective cases that occurred during summer 2009 in Beijing, China, are studied using the newly developed system. Results show that on average the assimilation of reflectivity significantly improves the short-term precipitation forecast skill up to 7 h. A diagnosis of the analysis fields of one case shows that the assimilation of reflectivity increases humidity, rainwater, and convective available potential energy in the convective region. As a result, the analysis successfully promotes the developments of the convective system and thus improves the subsequent prediction of the location and intensity of precipitation for this case.

1. Introduction

Radar reflectivity observations have been used to provide initial conditions for high-resolution numerical models through cloud analysis (e.g., Albers et al. 1996; Zhang et al. 1998; Souto et al. 2003; Hu et al. 2006). In cloud analysis schemes, the radar reflectivity observations are used to adjust the atmospheric variables, such as cloud condensates, hydrometeors, and in-cloud temperature (e.g., Albers et al. 1996; Zhang et al. 1998; Hu et al. 2006). A real-time implementation and one-month precipitation verification showed that the incorporation of a cloud analysis improved forecast of precipitation amount and spatial distribution (Souto et al. 2003). Besides the cloud analysis, other techniques such as Newtonian nudging and digital filters are also used to assimilate information derived from radar reflectivity observations (Michelson and Seaman 2000; Weygandt et al. 2008).

Radar reflectivity observations are also extensively used in variational data assimilation systems and ensemble Kalman filters (EnKF) to provide the best analysis for the high-resolution convective forecast. The potential of the EnKF's application to the convective scale was shown by assimilating simulated or real reflectivity observations (e.g., Dowell et al. 2004, 2011; Tong and Xue 2005, 2008; Xue et al. 2006; Jung et al. 2008; Aksoy et al.

* The National Center for Atmospheric Research is sponsored by the National Science Foundation.

Corresponding author address: Dr. Hongli Wang, National Center for Atmospheric Research, P. O. Box 3000, Boulder, CO 80307.
E-mail: hlwang@ucar.edu

DOI: 10.1175/JAMC-D-12-0120.1

2009, 2010). In EnKF, radar reflectivity is efficient to initialize both model hydrometeors and microphysics parameters associated with a microphysical scheme (Tong and Xue 2005, 2008; Jung et al. 2008). The three- and four-dimensional variational (3D-Var and 4D-Var) radar data assimilation systems have been developed and tested in research communities and operational centers. These systems include the Advanced Research and Prediction System 3D-Var (Gao et al. 2004; Gao and Stensrud 2012), the high-resolution radar data assimilation system at the Naval Research Laboratory (Zhao and Jin 2008), and the system using the 1D+3D-Var method at Météo-France (Caumont et al. 2010), the variational Doppler radar analysis system (Sun and Crook 1997), Japan Meteorological Agency's 4D-Var (Honda et al. 2005), and Weather Research and Forecasting (WRF) 4D-Var (Wang et al. 2011). These systems with differences in data assimilation implementation and numerical model all demonstrated potential impact of reflectivity observations in severe storm forecast (Sun 2005a). Although the 4D-Var and EnKF methods show great potential, these approaches still suffer from unaffordable computer costs for operational NWP at convection permitting–resolving scale. Thus, the 3D-Var and cloud analysis methods are still widely used in research communities and operational centers.

In the WRF (Skamarock et al. 2008) model's three-dimensional variational data assimilation system (WRF 3D-Var; Barker et al. 2004, 2012), Xiao et al. (2007) developed a direct radar reflectivity data assimilation scheme. This approach uses model total water mixing ratio as the moisture control variable and a warm-rain partition scheme to split it into water vapor, cloud water, and rainwater. The results from the study of a convective case reported by Xiao and Sun (2007) showed while the quantitative precipitation forecast (QPF) was improved by the assimilation of both radial velocity and reflectivity, the impact of reflectivity alone had mixed results.

In this paper, we will show that one of the problems with the direct reflectivity data assimilation in WRF 3D-Var lies in the use of a linearized Z–q_r (reflectivity–rainwater) equation [see Eq. (3) in section 2] as the observation operator and of the warm-rain partition scheme. The WRF 3D-Var applies the incremental approach as proposed by Courtier et al. (1994) that requires the linearization of the forward model. The logarithm Z–q_r equation has a high degree of nonlinearity especially when q_r is small (i.e., a "dry" first guess relative to observations), which can lead to large linearization errors. (A detailed analysis will be given in section 2b). The problem of "dry" first guess can affect the partition of the microphysics because the switches that initiate the warm-rain processes may never be turned on during the minimization of the cost function. To circumvent the problem, in some studies using WRF 3D-Var, physical initialization (Yang et al. 2006) or cloud analysis procedures (Sugimoto et al. 2009) were carried out before assimilating radar reflectivity.

In this paper, we present an indirect radar reflectivity assimilation scheme in the framework of WRF 3D-Var. This scheme, instead of directly assimilating radar reflectivity, assimilates retrieved rainwater and water vapor derived from radar reflectivity. It will be shown that the assimilation of the retrieved rainwater eliminates the observation operator necessary in the direct assimilation of reflectivity and thus avoids the problem caused by the linearization of the operator. Additionally, the assumption that the in-cloud humidity is saturated (Albers et al. 1996; Zhang et al. 1998) is used to produce an estimate of the saturated water vapor "observations." A new observation operator is introduced to assimilate the estimated water vapor. The assimilation of the estimated water vapor is expected to provide a favorable environment that supports convection.

This scheme is tested in a Rapid Update Cycle data assimilation and forecast system operating at Beijing Meteorology Bureau (BMB) since 2008 (named BJ-RUC; Chen et al. 2009) using four heavy-rain-producing convective cases occurred in the Beijing region during summer 2009. The paper is organized as follows: section 2 provides a description of the WRF 3D-Var, an analysis of the linearization error of the Z–q_r equation, and the description of the methodology of the newly developed WRF 3D-Var radar reflectivity assimilation scheme. Experimental configuration is presented in section 3. Results are described in section 4. A summary and conclusion are presented in the final section.

2. Methodology

a. WRF 3D-Var

The WRF 3D-Var adopts the incremental variational formulation that is commonly used in operational systems. The incremental approach minimizes a cost function defined as a function of the analysis increment relative to the background by using a linearized observation operator:

$$J = J_b + J_o = \frac{1}{2}\mathbf{v}^{\mathrm{T}}\mathbf{v} + \frac{1}{2}(\mathbf{d} - H'\mathbf{U}\mathbf{v})^{\mathrm{T}}\mathbf{R}^{-1}(\mathbf{d} - H'\mathbf{U}\mathbf{v}), \qquad (1)$$

where J_b stands for the background term and J_o is the observation term. Their specific forms in the incremental formulation are represented in the second line of Eq. (1). The term $\mathbf{v}$ is the control variable (CV) defined

by $\mathbf{v} = \mathbf{U}^{-1}(\mathbf{x} - \mathbf{x}_b)$, where $\mathbf{U}$ is the decomposition of the background error covariance $\mathbf{B}$ under the constraint $\mathbf{B} = \mathbf{U}\mathbf{U}^{\mathrm{T}}$, $\mathbf{x}$ is the full analysis variable, and $\mathbf{x}_b$ is the background variable. The quantity $\mathbf{d} = \mathbf{y}^o - H(\mathbf{x}_b)$ is the innovation vector that measures the departure of the observation $\mathbf{y}^o$ from its counterpart computed from the background $\mathbf{x}_b$, H' is the linearization of the nonlinear observation operator H, and $\mathbf{R}$ is observation error matrix. The new development described in this paper is made with the CV option 5 in WRF 3D-Var, which uses the streamfunction, unbalanced velocity potential, unbalanced temperature, unbalanced surface pressure, and pseudo–relative humidity as the control variables. The word "unbalance" refers to the residual from the balance with the streamfunction. In this study, a new control variable, that is, rainwater mixing ratio, is added.

b. Validity of linearized Z–q_r equation

Since the incremental formulation is used in the WRF 3D-Var system, the linearized Z–q_r equation is employed as the observation operator to assimilate radar reflectivity in a direct method. In this section, the validity of the linearized Z–q_r equation is analyzed to determine the error characteristics of the linearization.

The nonlinear Z–q_r relation (Sun and Crook 1997) is

$$Z = c_1 + c_2 \log_{10}(\rho q_r), \tag{2}$$

where Z is the reflectivity (dBZ); c_1 and c_2 are constants with the value of 43.1 and 17.5, respectively; ρ is the air density (kg m^{-3}); and q_r is the rainwater mixing ratio (g kg^{-1}). Equation (2) is used as the nonlinear observation operator H to calculate the innovations.

The linearized formulation of Eq. (2) is

$$dZ = \frac{c_2 dq_r}{q_r \ln(10)}. \tag{3}$$

Equation (3) was used as the observation operator H' to assimilate the reflectivity in Xiao and Sun (2007). It is seen that Eq. (3) is invalid when there is no rainwater in the first guess. This may cause the difficulty in convergence of a cost function because of a large gradient wherever the rainwater is very small (Sun and Crook 1997). In the following analysis, it is shown that the linearized Eq. (3) has large discrepancy from its nonlinear form, especially when the background is too dry compared with observations.

Assuming an increment of rainwater dq_r is added to the background rainwater q_r, the resulting reflectivity can be obtained from Eq. (2):

$$Z_{\mathrm{new}} = c_1 + c_2 \log_{10}[\rho(q_r + dq_r)]. \tag{4}$$

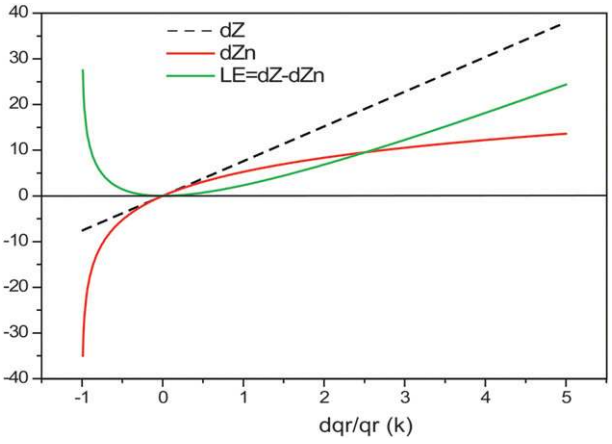

FIG. 1. Linear perturbation dZ, nonlinear difference dZ_n, and the LE–k relation.

The perturbation of the reflectivity caused by dq_r is

$$dZ_n = Z_{\mathrm{new}} - Z = c_2 \log_{10}[(q_r + dq_r)/q_r] \tag{5}$$

with $dq_r/q_r = k$. The linear approximation error (LE) is the difference between Eqs. (5) and (3):

$$\mathrm{LE} = dZ - dZ_n = \frac{c_2 k}{\ln(10)} - c_2 \log_{10}(1 + k). \tag{6}$$

Equation (6) is called the LE–k relation, which shows that the validity of the linear Z–q_r equation only depends on the ratio k of the rainwater increment to the basic-state rainwater. The numerical solution of Eq. (6) is shown in Fig. 1. It is seen that a difference between the linear (dashed line) and nonlinear (red curve) solutions is that the former is physically truncated at $k = -1.0$ but the latter is not. Figure 1 also reveals that the larger the absolute k is, the less valid is the tangent-linear assumption. For example, if the background q_r is 0.1 g kg^{-1}, and the increment dq_r is 0.5 or -0.1 g kg^{-1}, the corresponding k is 5 or -1, resulting in a linear approximation error larger than 20 dBZ (Fig. 1). In these cases, the linearized observation operator is not an acceptable approximation to the nonlinear one. It is common that convective forecasts have displacement errors, which means it is typical for k to be close to -1 or larger than 5 (especially when the background is too dry in comparison with observations), causing significant linearization errors. Figure 1 also shows that LE is always larger than 0.0, meaning dZ always overestimates dZ_n. Conversely, when fitting an innovation of radar reflectivity with the linearized Z–q_r equation, for the same background rainwater q_r, an underestimated increment of rainwater dq_r (dry bias) is obtained relative to the increment derived from the nonlinear Z–q_r equation. For example, if there

is an innovation of 10.0 dBZ, the k from the nonlinear relation is 2.73, whereas from the linearized relation is 1.32.

c. Assimilating retrieved rainwater and water vapor

The above analysis clearly indicates that the linearization of the Z–q_r relation results in significant errors in certain circumstances. It implies that when the model forecast has a large deviation from the observation, the optimal solution derived from the linearized and nonlinear observation operators can be very different. To handle this problem, we suggest assimilating the retrieved rainwater from radar reflectivity instead of directly assimilating the reflectivity. The rainwater is retrieved from the radar reflectivity before the data assimilation, thereby eliminating the reflectivity observation operators required in the direct assimilation avoiding the problem caused by the linearization of the operator. Given a reflectivity observation, the rainwater retrieval is calculated by using Eq. (2). The air density ρ is derived from first guess. Equation (3) is used to specify the error of rainwater given the reflectivity error obtained from the radar preprocessing and quality control procedure (Sun 2005b; Lim and Sun 2010). It is noted that the empirical Z–R relationship like Eq. (2) may cause large bias in retrieved rainwater content, especially for strong convective region where large amount of hail–graupel exist. To reduce this error in nonlinear observation operator, rainwater retrieval is calculated only when the reflectivity is smaller than 55 dBZ in this study.

In this paper, the assumption that the in-cloud humidity is saturated, which is commonly used in cloud analysis schemes (Albers et al. 1996; Zhang et al. 1998), is used to produce an estimate of the saturated water vapor observation. The assimilation of the estimated water vapor is expected to provide a favorable environment that supports convection.

To assimilate retrieved rainwater and water vapor, the following two additional terms are added into Eq. (1):

$$J_{\rm qr}=\frac{1}{2}(\mathbf{q}_r-\mathbf{q}_r^b)^{\rm T}\mathbf{B}_{\rm qr}^{-1}(\mathbf{q}_r-\mathbf{q}_r^b)+\frac{1}{2}(\mathbf{q}_r-\mathbf{q}_r^o)^{\rm T}\mathbf{R}_{\rm qr}^{-1}(\mathbf{q}_r-\mathbf{q}_r^o) \tag{7}$$

and

$$J_{\rm qv}=\frac{1}{2}(\mathbf{q}_v-\mathbf{q}_v^o)^{\rm T}\mathbf{R}_{\rm qv}^{-1}(\mathbf{q}_v-\mathbf{q}_v^o), \tag{8}$$

where $\mathbf{q}_r$ and $\mathbf{q}_v$ represent the rainwater and water vapor of the atmospheric state, respectively; $\mathbf{q}_r^o$ and $\mathbf{q}_v^o$ are the retrieved rainwater and water vapor from radar reflectivity observations; and $\mathbf{R}_{\rm qr}$ and $\mathbf{R}_{\rm qv}$ are the observation error variance of rainwater and water vapor, respectively. The rainwater is introduced as the new control variable, so that there is a background term in Eq. (7). The background term for $\mathbf{q}_v$ is the same as in the standard WRF 3D-Var without radar data assimilation, so it is not written in Eq. (8). The quantities $\mathbf{q}_r^b$ and $\mathbf{B}_{\rm qr}$ are the background rainwater and background error matrix of rainwater, respectively. The specification of $\mathbf{B}_{\rm qr}$ will be described in the next section.

In the following, the retrieval and assimilation of the water vapor will be described. The in-cloud relative humidity assumed to be 100% where radar reflectivity is higher than a threshold above cloud base, so that the estimated water vapor, used as the ''observation'' $\mathbf{q}_v^o$ in Eq. (8), equals to the saturation water vapor that is calculated based on the pressure and temperature of the background. In this paper the threshold is set to 30 dBZ. The error of the water vapor observation is specified by the relative humidity error with a constant value of 20%. It is noted that there are two sources of uncertainties in the current retrieval method. The first is the identification of ''cloud'' region, and the second is the calculation of saturated water vapor, whose accuracy depends on the quality of pressure and temperature fields in first guess. It is pointed out that the background error modeling of relative humidity also plays an import role in saturated water vapor assimilation.

It is straightforward to convert Eq. (7) into its incremental form as represented in the second line of Eq. (1) because $\mathbf{q}_r$ is a model variable as well as a control variable. For the new observation term of $\mathbf{q}_v$ given by Eq. (8), the nonlinear observation operator H is defined by

$$q_v = {\rm rh}\times q_s, \tag{9}$$

where q_v, rh, and q_s stand for specific humidity, relative humidity, and saturated specific humidity of water vapor, respectively. Equation (9) links the water vapor to the control variable rh and then to the control variables temperature and pressure through Eqs. (11) and (12) below. It is physically reasonable that the perturbation in humidity affects pressure and temperature under the condition that moisture is close to saturation, where thermal processes take place by phase conversions between water vapor and cloud condensates (Bannister 2008).

The linear observation operator H' of Eq. (9) is

$$dq_v = d{\rm rh}\times q_s + {\rm rh}\times dq_s, \tag{10}$$

where

$$q_s=\frac{\varepsilon e_s}{p-(1-\varepsilon)e_s}, \tag{11}$$

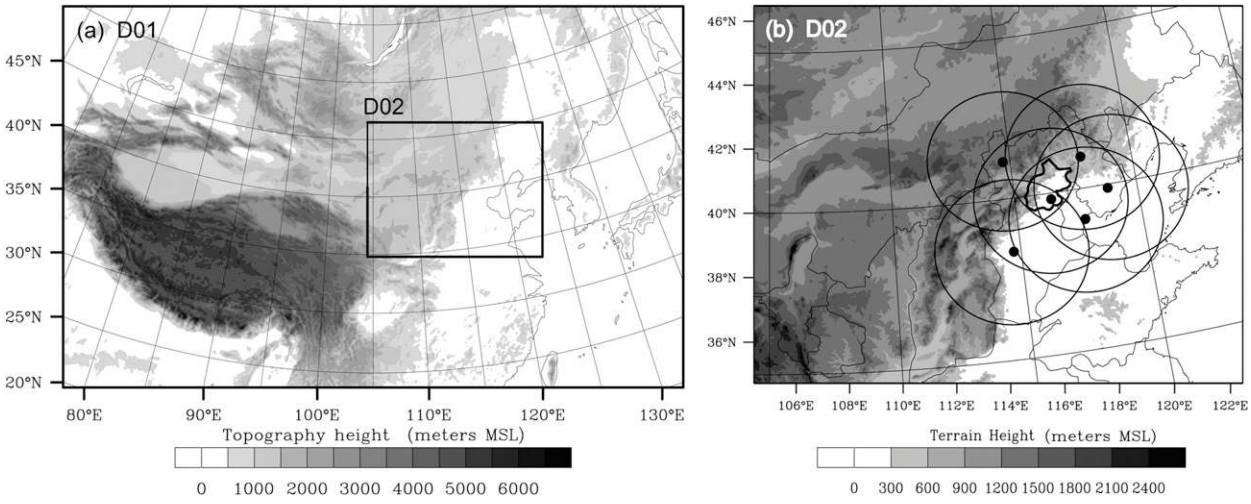

FIG. 2. Model domains superposed with topography (m) for (a) outer and inner domains (D01 and D02), and (b) inner domain (D02). The black dots show the locations of the six radar stations. The thick black outlined irregular area in (b) shows the border of Beijing city.

$$e_s = c_1 \exp\left(\frac{c_2 T}{T + c_3}\right), \tag{12}$$

$\varepsilon = 0.622$, $c_1 = 6.112$, $c_2 = 17.67$, and $c_3 = 243.5$.

Using Eqs. (11) and (12), Eq. (10) can be rewritten as

$$dq_v = q_s \times d\mathrm{rh} + \mathrm{rh} \times \left(\frac{\partial q_s}{\partial p} dp + \frac{\partial q_s}{\partial e_s}\frac{\partial e_s}{\partial T} dT\right). \tag{13}$$

By neglecting the contribution of pressure perturbation on saturated water vapor variation in Eq. (13), the final linearized observation operator is simplified as

$$dq_v \approx q_s \times d\mathrm{rh} + c_4 q_v dT, \quad \text{and} \quad c_4 = \frac{c_2 c_3}{(T + c_3)^2}. \tag{14}$$

Note that c_4 is always larger than 0, so that when the saturation water vapor is assimilated, positive relative humidity and temperature increments will be obtained. Note that a similar function has been applied in cloud analysis schemes (Zhang et al. 1998), in which the background moisture (if it is undersaturated) is increased and latent heat is added wherever cloud exists.

3. Experimental configuration

a. BJ-RUC system

The BJ-RUC system (Fan et al. 2008; Chen et al. 2009) includes the WRF 3D-Var system (version 3.3) and the WRF model (version 3.3.1). It has been run in operation at BMB since June 2008 (Chen et al. 2009). The model physics options in BJ-RUC include the Rapid Radiative Transfer Model longwave radiation, Goddard shortwave radiation, Yonsei University PBL schemes, and WRF single-moment six-classes microphysics (WSM6). Descriptions of the above physical process schemes can be found in the WRF technical report by Skamarock et al. (2008). BJ-RUC employs a one-way, two-domain nested grid. The model domains and the six radar station locations are shown in Fig. 2. The outer model domain covers China's mainland, and the inner domain covers Beijing and its surrounding region. The horizontal grid resolutions of the outer and inner domains are 9 and 3 km, respectively. There are 38 full eta levels in the vertical.

The procedure of BJ-RUC is as follows. The BJ-RUC employs a 3-hourly partial cycling strategy. First, two 72-h forecasts for the outer domain are made at 0000 and 1200 UTC each day. The initial and boundary fields are interpolated from National Centers for Environmental Prediction (NCEP) Global Forecast System (GFS) 1° × 1° analyses and forecasts for these two runs, which then provide the boundary conditions for the inner domain. The 3-hourly rapid update cycling is run in this inner domain. The 3-h forecast of the inner domain initiated from the GFS analysis at 0000 UTC provides the first guess for the 0300 UTC 3D-Var analysis. Then, the 3-h WRF forecast from the current analysis provides the first guess for the next analysis. A 12-h forecast is made starting from each analysis.

The conventional data, such as radiosondes, synops, and aircraft reports, as well as global positioning system precipitable water have been ingested into BJ-RUC since 2008. Preliminary tests for the assimilation of radar observations suggested that the radar reflectivity

TABLE 1. Descriptions of the four convective cases.

Date	Lifetime (UTC)	Description	Radar data available period (UTC)
14 Jun	0530–1200	Local convection	0600–1200
11 Jul	0230–1800	Local convection	0300–1200
22 Jul	0430–1500	Convective systems moved from north of Beijing city	0600–1200
23 Jul	0330–1700	Squall line moved from northwest of Beijing city	0300–1200

assimilation using the direct scheme developed by Xiao et al. (2007) had insignificant impact (S. Fan 2011, unpublished manuscript), which motivated us to develop the new scheme presented in this paper. The indirect assimilation of reflectivity observations described in this study will be implemented in the BJ-RUC data assimilation system to further improve the very short-term (0–6 h) precipitation forecast. The radial wind assimilation scheme used in this paper was developed by Xiao et al. (2005). Readers can refer to that paper for details.

The so-called National Meteorological Center (NMC) method (Parrish and Derber 1992) was used to generate the background error statistics using the utility packages in the WRF 3D-Var system. The NMC method was first tested for research purposes (Fang et al. 2006) and then employed in the operational BJ-RUC system. A set of cold start forecasts over the inner domain were initiated from NCEP GFS $1° \times 1°$ final (FNL) analysis at 0000 and 1200 UTC every day during August 2008. The differences between the 24- and 12-h forecasts valid at same times were used to calculate the domain-averaged background error statistics (except for rainwater mixing ratio). By some trial-and-error experiments we found the rescaling factor of 0.5 for variance scale and length scale produced improved analysis and forecast. For the rainwater, only the horizontal correlation is considered, and the variance is set to 4.0 g kg^{-1} and the length scale is set to 10.5 km.

b. Convective cases

The four warm season convective cases that are selected for this study are summarized in Table 1. The first two are locally developed convective systems within the Beijing region (the border is marked by bold black in Fig. 2a); the other two are convective systems moved into Beijing. Sun et al. (2005) showed that heavy rainfall in Beijing took place in a favorite synoptic environment that associated with low-level vortex and midlevel low pressure systems. Figure 3 shows the geopotential height at 500 hPa, and wind vector and relative humidity at 750 hPa from GFS FNL analyses at 0600 UTC (1400 local time) for the four cases. For the 14 June case, it is seen that there was a low pressure system (marked by "L" in Fig. 3a) at 500 hPa and an associated cyclonic vortex system (marked by "D" in Fig. 3a) at 750 hPa northeast to Beijing. Beijing is located in a convergence region forced by the flows in front of two trough systems at 750 hPa (lines A–B and A2–B2 in Fig. 3a), which are related to the low-level vortex system at 750 hPa. As for the 11 July case, there is a low pressure system and an associated cyclonic vortex system (marked by "L" and "D" in Fig. 3b) at 750 hPa northwest to Beijing. The convective system took place in front of the trough associated with the low-level vortex system (Fig. 3b). A horizontal wind shear (line E–F in Fig. 3b) may also contribute to the initiation of the convective system. For the 22 and 23 July cases, there are two low pressure systems at 500 hPa and two associated vortex systems at 750 hPa (Figs. 3 and 4). For the 22 July case, the convective system was initiated in front of a trough at 750 hPa (Fig. 3c). The low pressure and vortex systems in upstream of Beijing on 22 July ("L2" and "D2" in Fig. 3c) moved rapidly and reached north of Beijing on 23 July ("L2" and "D2" in Fig. 3d), which results in a heavy precipitation event in Beijing. In addition, for the four cases, Beijing is located in or close to the region where relative humidity values are larger than 70%. To summarize, the convective systems of the four cases are initiated in front of trough systems that are associated with low-level vortex systems.

c. Radar data and experimental setup

The preprocessing and quality control of Doppler radar data are the same as that described in Sun (2005b). The data are thinned to 3-km resolution. The available period of radar data for each case is listed in Table 1. An hourly radar quantitative precipitation estimate (QPE) that is produced operationally at BMB is taken as the observation for verifying the model forecasts.

Four numerical experiments (Table 2) are conducted to examine the impact of radar observations on analysis and precipitation forecast for each of the four cases. In the control experiment (CON), only the conventional observations are assimilated. The experiment CRW (CRV) assimilates radar retrieved rainwater and water vapor (radar radial velocity) observations in addition to the conventional observations. The experiment ALL assimilates all observations used in the above experiments. In

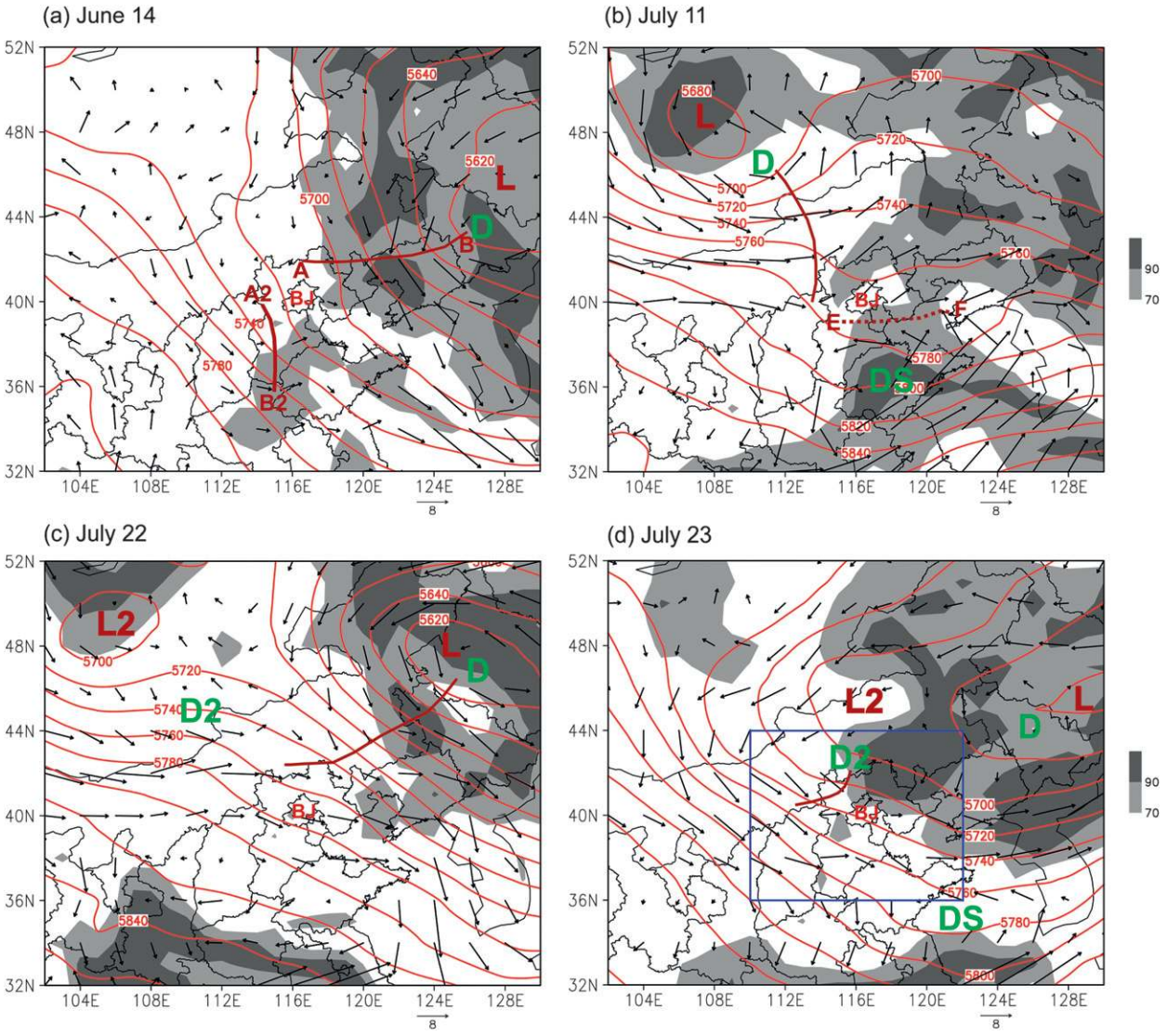

FIG. 3. Horizontal distribution of relative humidity (shaded; %), wind vectors (m s^{-1}) at 750 hPa and geopotential height (red contours) at 500 hPa from NCEP FNL analyses at 0600 UTC for case (a) 14 Jun, (b) 11 Jul, (c) 22 Jul, and (d) 23 Jul. "L" and "L2" represent low pressure systems at 500 hPa. "D" and "D2" represent the low-level vortex systems at 750 hPa. "BJ" indicates the location of Beijing region. The dark red line represents a trough line or convergence line. The blue rectangles show the domain on which diagnosis for case 23 Jul is conducted in section 4b.

the experiments CRV and ALL, we only assimilate the radial velocity where the reflectivity has values larger than or equal to 15 dB*Z*.

4. Results

a. Single reflectivity observation test

Before conducting the real data experiments, a single reflectivity observation assimilation test is carried out to estimate the spread of observation information by background error statistics and the response of the new observation operators. The first guess is interpolated from GFS final analysis at 0600 UTC 22 July 2009. The single reflectivity observation is assumed at (39.9°N, 116.0°E; 20th model level). The innovation (observation minus background) of the single reflectivity is assigned to 10 dB*Z*, which is about 1.0 g kg^{-1} when converted to rainwater. The error of the single reflectivity is set to 10 dB*Z*.

Figure 4 shows the responses of the 3D-Var analysis increment at the 20th model level (approximate 700 hPa). First of all, the rainwater mixing ratio and water vapor mixing ratio have positive analysis increments centered at

TABLE 2. List of experiments.

Expt	Description
CON	Conventional observation
CRV	Conventional observation + radial velocity
CRW	Conventional observation + retrieved rainwater + derived water vapor
ALL	Conventional observation + radial velocity + retrieved rainwater + derived water vapor

the observation location (Figs. 4a,b). The maximum values of rainwater and water vapor mixing ratio are 0.73 and 1.2 g kg^{-1}, respectively. The positive increment arises because the two variables are underestimated in the first guess. The water vapor spreads broader than the rainwater since the length scale of the water vapor is larger than the rainwater. The temperature increment is a result of the water vapor assimilation (Fig. 4c), as indicated by Eq. (14). However, the maximum of potential temperature increment is about 0.041 K, which is pretty small. One reason of the small temperature increment is that the current domain-averaged background error statistics (CV5) tends to underestimate temperature uncertainties in rain regions. Through the wind and temperature statistical relation in the background error covariance, the wind response is obtained (Fig. 4d). Although the single reflectivity observation has a small impact on wind and temperature variables, the indirect assimilation scheme is capable of producing a multivariate analysis.

b. Results of the Beijing cases

We first examine the average forecast skill of the hourly accumulated precipitation from the four cases. The neighborhood-based fractions skill score (FSS) is

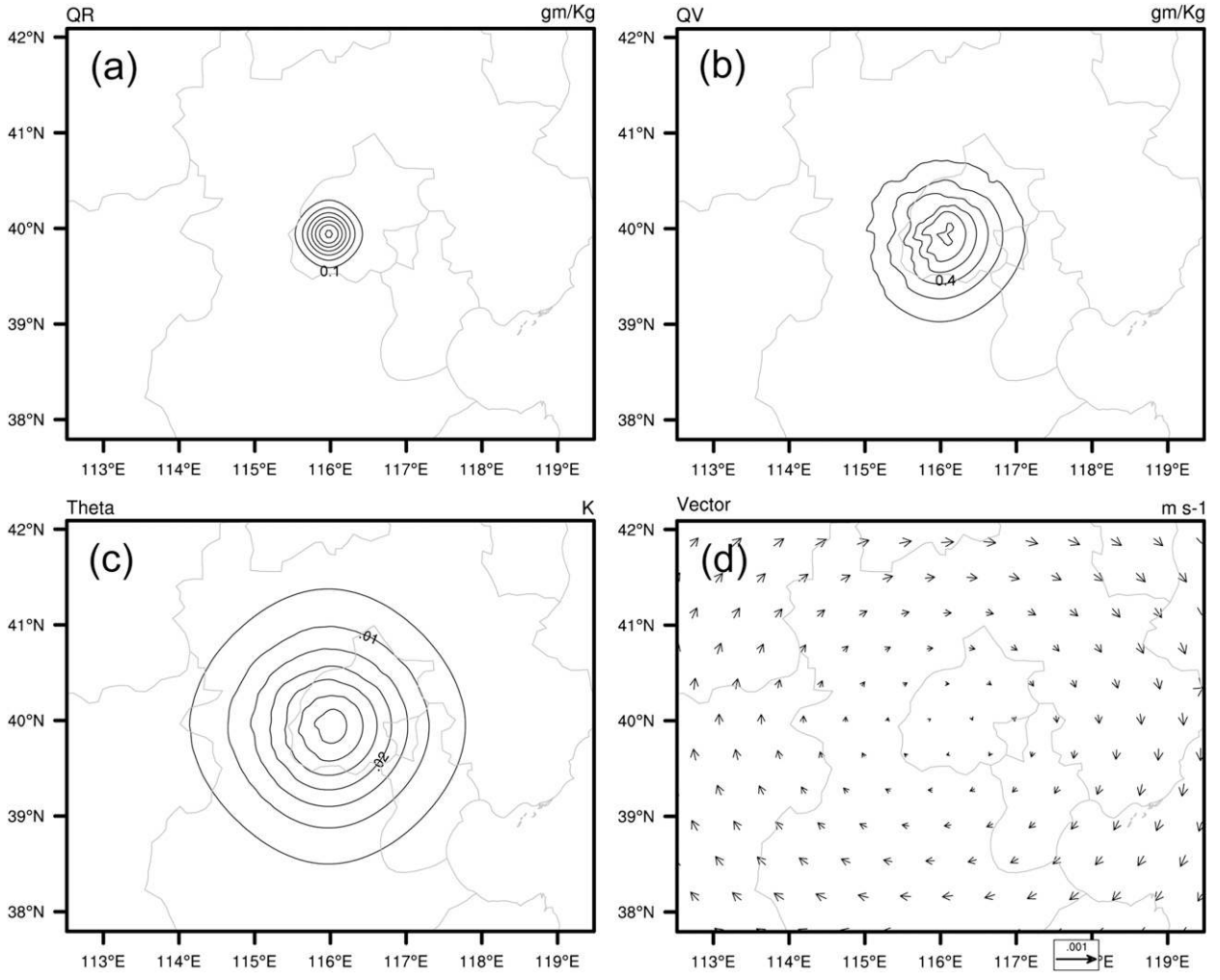

FIG. 4. Increments from the single observation test for (a) rainwater mixing ratio (interval is 0.1; g kg^{-1}), (b) water vapor mixing ratio (interval is 0.2; g kg^{-1}), (c) potential temperature (interval is 0.05; K), and (d) wind vectors (m s^{-1}).

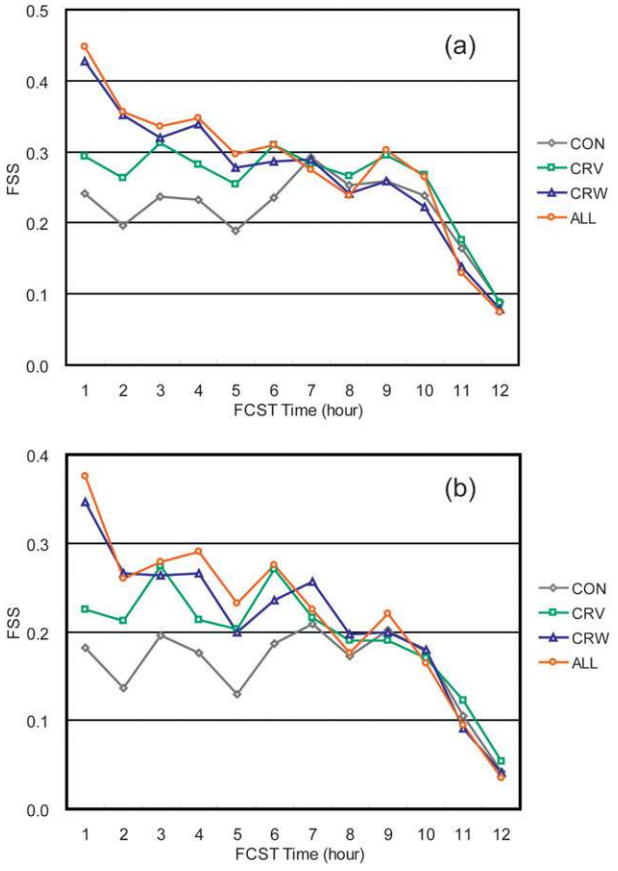

FIG. 5. Averaged FSS of the four experiments for thresholds of (a) 5 mm h^{-1} and (b) 10 mm h^{-1}.

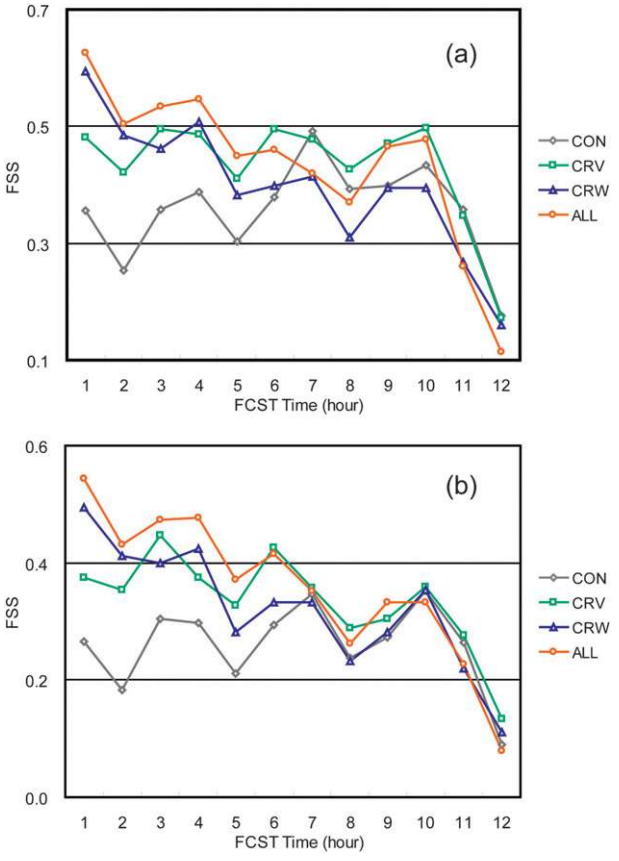

FIG. 6. Averaged FSS of the 23 Jul case for thresholds of (a) 5 mm h^{-1} and (b) 10 mm h^{-1}.

used for the verification. The FSS is defined by the formulation (Roberts and Lean 2008)

$$\mathrm{FSS} = 1 - \frac{\frac{1}{N}\sum_{N}(P_f - P_o)^2}{\frac{1}{N}\left(\sum_{N} P_f^2 + \sum_{N} P_o^2\right)}, \qquad (15)$$

where P_f and P_o are the forecasted and observed fractional coverage of an elementary area by rainfall that exceeds a given threshold value, and N gives the number of grid points in the verification domain. If a precipitation prediction is perfect, which means P_f is equal to P_o, then FSS is 1.0.

There are a total of 16 analyses and forecasts from the four cases. Radar observations are assimilated in 14 of the 16 analyses, because radar data were not collected at 0300 UTC 14 June 2009 and 0300 UTC 22 July 2009. Therefore, only the 14 forecasts are included in the following FSS evaluation.

Figures 5a and 5b show the averaged FSS of the four experiments. When compared with experiment CON all the radar data assimilation experiments improve the FSS up to 7 h for the thresholds of 5.0 and 10 mm h^{-1}. The experiment CRW has more positive impact than the experiment CRV in the first 5 h. The experiment ALL produces the best skill in the first 6 h. After a 7-h forecast, the impact of radar data assimilation is neutral. When forecasts for each convective case are examined, it is found that CRW shows consistent improvement over CRV in the first 5–6 h while CRV produces a slightly degraded FSS than CON in the first 5 h for the case on July 11 for both thresholds (figures not shown).

Next we conduct a detailed examination for the case of 23 July. This case took place in a typical synoptic environment for Beijing heavy rainfall events as described in section 3b. It produced a large amount of precipitation, resulting in a local flood in Beijing. The FSS for this case, shown in Figs. 5a and 6b, suggest that CRW produces better forecasts than CON in the first 6 h and CRV improves the forecast skill over CON up to 12 h for the thresholds of 5 and 10 mm h^{-1}. When reflectivity (retrieved rainwater and derived water vapor) is assimilated together with the radial velocity in ALL, the

precipitation forecast is slightly improved over CRV in the first 5 h for both thresholds.

By examining precipitation patterns subjectively, we have found that the experiments CRW and ALL produce precipitation patterns that are closest to the observations. Figure 7 shows the hourly radar QPE and precipitation forecasts at 0900 and 1000 UTC from the four experiments for the case of 23 July. It is seen that the experiment CON produces a weak and broken precipitation band and misses the intense precipitation in the Beijing central district at 0900 UTC. CRV has slightly improved forecasts. The experiments CRW and ALL give the best precipitation forecasts of the major convective system over Beijing in both the location and intensity, suggesting that the indirect reflectivity assimilation method is effective to correct the location error in the background field.

A diagnosis of the analysis fields of the 23 July case is carried out to assess reasons leading to the improved forecast. This is done by comparing the analyses from different experiments. Figure 8 shows the analyses of the experiments CON, CRV, CRW, and ALL for the 23 July case from the second cycle at 0600 UTC 23 July 2009. From the analyses of the wind and relative humidity at 750 hPa and the geopotential height at 500 hPa (Figs. 8a,c,e,g) and the rainwater analyses at 750 hPa (black contours in Fig. 8h), it is seen that the rainfall event occurred in the region ahead of a trough system with a high relative humidity. Relative to CON (Fig. 8a), the assimilation of radial velocity (CRV and ALL; Figs. 8b,c) increases the low-level southwest jet from 10 to 12 m s^{-1} to transport the moisture to support the convective system. The indirect reflectivity assimilation increases the relative humidity in the convective region, which can be seen by comparing CRW (Fig. 8e) or ALL (Fig. 8g) with CON (Fig. 8a) or CRV (Fig. 8c). As a result, the convective available energy is increased as seen by comparing CRW (Fig. 8f) or ALL (Fig. 8h) with CON (Fig. 8b) or CRV (Fig. 8d). The rainwater analyses from CON and CRV (Figs. 8b,d) show that the convective system occurs in these two experiments but evidently is not as strong and extensive as that in CRW (Fig. 8f) and ALL (Fig. 8h). The above analysis shows that the assimilation of reflectivity data increases the relative humidity, rainwater, and convective available potential energy in the convective region. These analysis adjustments through radar data assimilation provide a favorable environment for the development and maintenance of the convective system.

5. Summary and conclusions

In this study, an indirect radar reflectivity assimilation scheme is developed within the WRF 3D-Var system. The scheme assimilates retrieved rainwater and water vapor derived from radar reflectivity. The corresponding observation operators for rainwater and saturated water vapor are developed and incorporated into the WRF 3D-Var. The validity analysis of the linearized Z–q_r (reflectivity–rainwater) equation shows that it can produce a dry bias in rainwater analysis and results in significant linearized errors in certain circumstances. The moisture field which plays an important role in the improvement of the precipitation is also changed through this scheme.

The scheme is first tested by a single reflectivity observation experiment and then data assimilation experiments with real data. The results show that a single reflectivity observation produces the multivariate analysis in the indirect assimilation scheme. Four heavy-rain-producing convective cases occurred in the Beijing region during summer 2009 are studied with observed radar data using the operational system BJ-RUC. The results show that, on average, the assimilation of reflectivity data improves the QPF skill up to 7 h as measured by the fractions skill score. The case that occurred on 23 July is selected to examine how the reflectivity assimilation adjusts the analysis and hence improves the forecast. It is shown that the assimilation of reflectivity data increases the moisture, rainwater, and CAPE in the initial fields. The analysis can successfully promote the developments of the convection in the region covered by radar observations and improve the subsequent forecasts of the location and intensity of the convective systems. Further work will focus on development of a more sophisticated method to estimate the in-cloud humidity from radar reflectivity.

It is worth noting that for microphysical variables the current study only considers the analysis and initialization of rainwater. The indirect method presented in this study can be extended to the analysis and initialization of other hydrometeor variables such as snow and hail. Gao and Stensrud (2012) presented a method for the reflectivity assimilation to include the analyses of ice hydrometeors in which empirical relations between reflectivity and snow and between reflectivity and hail were used for these hydrometeors. We plan to apply these similar relations to retrieve the snow and hail in our indirect assimilation scheme and add the assimilation of these microphysical fields in our future study. In addition, dual-polarization radar measurements can be used to identify hydrometeor types (Marzano et al. 2006) because the dual-polarization radar measurements of precipitation are sensitive to the hydrometeor properties such as shape, orientation, size, phase state, and fall behavior (Lim et al. 2005).

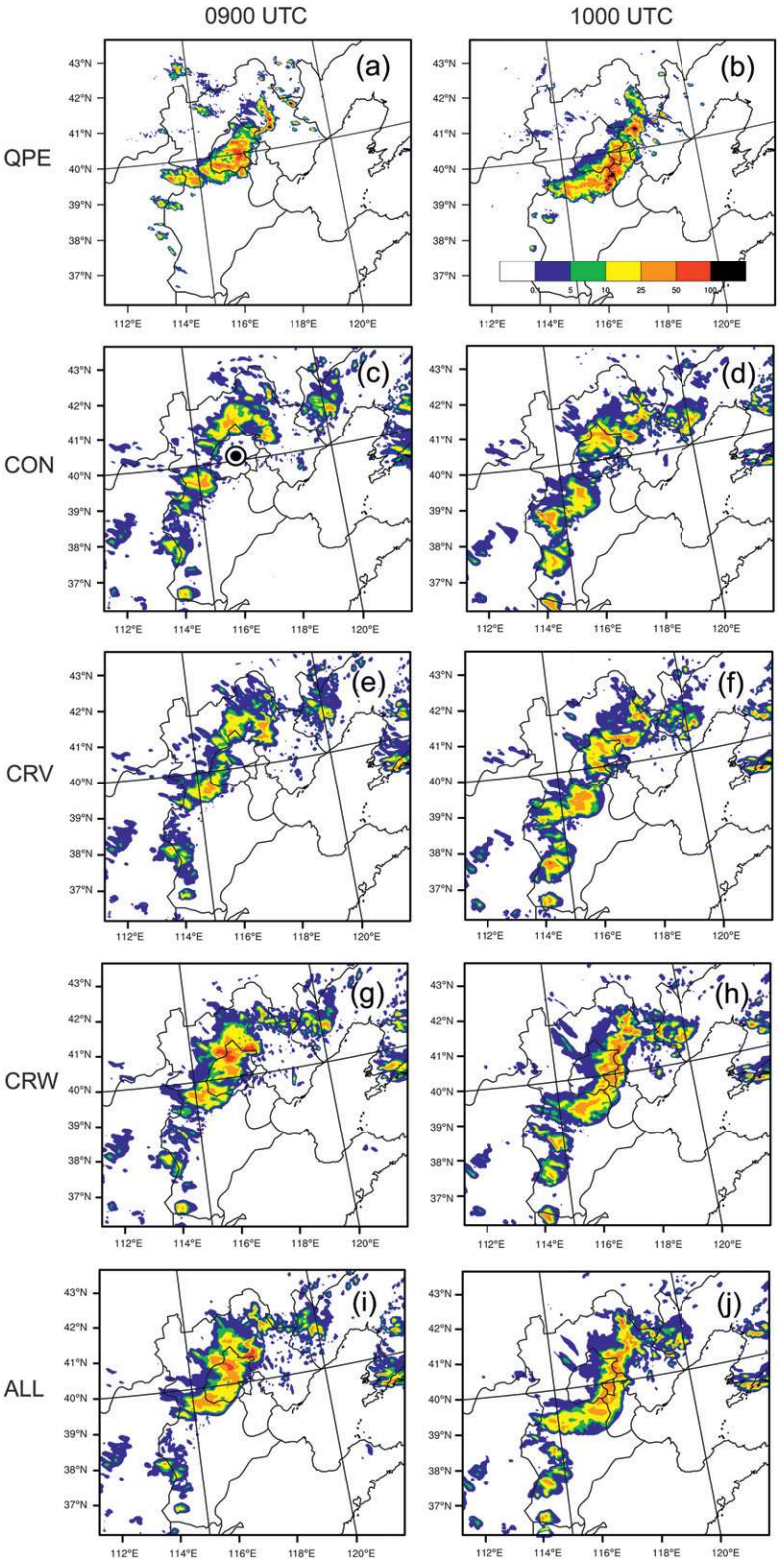

FIG. 7. Hourly accumulated precipitation (mm) for the case on at (left) 0900 UTC 23 Jul and (right) 1000 UTC from (a),(b) radar QPE, and the experiments (c),(d) CON, (e),(f) CRV, (g),(h) CRW, and (i),(j) ALL. The forecast starting time is 0600 UTC 23 Jul 2009. The city center of Beijing is marked by a black dot and circle in (c).

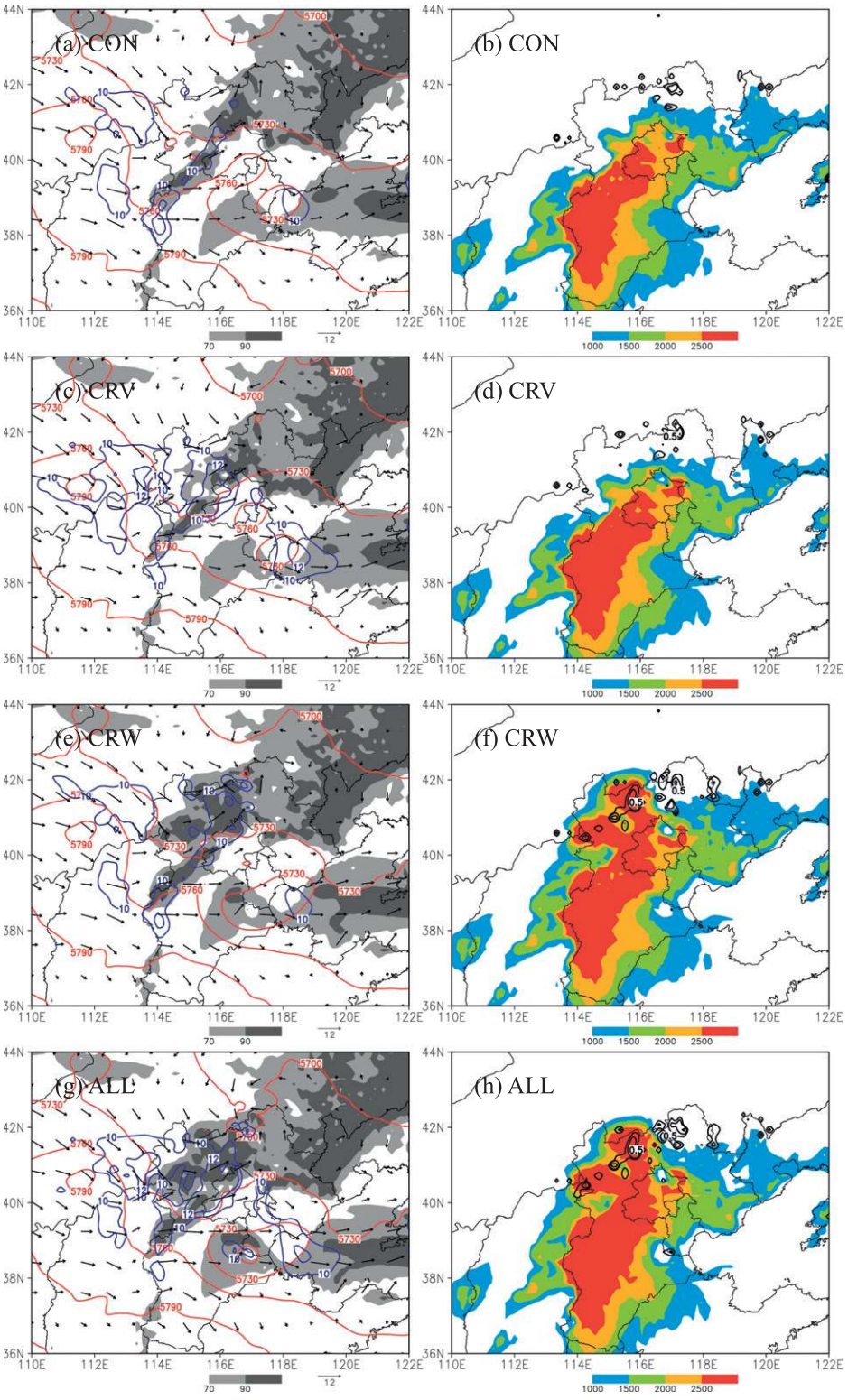

FIG. 8. (left) Horizontal distribution of relative humidity (shaded; %), superposed with wind vectors and speeds (blue contour; m s^{-1}) at 750 hPa and geopotential height (red contours) at 500 hPa of analyses from the experiments (a) CON, (c) CRV, (e) CRW, and (g) ALL. (right) Horizontal distribution of maximum convection available potential energy (shaded; J kg^{-1}) and rainwater mixing ration (black contours; g kg^{-1}) from experiments (b) CON, (d) CRV, (f) CRW, and (h) ALL. The valid time is 0600 UTC 23 Jul 2009.

Acknowledgments. This work was supported through funding from the National Science and Technology Supporting Programs of China in the 11th Five-Year Plan (Grant 2008BAC37B03), the National Science Foundation's U. S. Weather Research Program (USWRP), and the Institute of Urban Meteorology, Beijing, China. We thank Dr. Glen Romine for the helpful comments on an earlier version of this manuscript. Any opinions, findings, and conclusions or recommendations expressed in this publication are those of the authors and do not necessarily reflect the views of the National Science Foundation.

REFERENCES

Aksoy, A., D. C. Dowell, and C. Snyder, 2009: A multicase comparative assessment of the ensemble Kalman filter for assimilation of radar observations. Part I: Storm-scale analyses. *Mon. Wea. Rev.,* **137,** 1805–1824.

——, ——, and ——, 2010: A multicase comparative assessment of the ensemble Kalman filter for assimilation of radar observations. Part II: Short-range ensemble forecasts. *Mon. Wea. Rev.,* **138,** 1273–1292.

Albers, S. C., J. A. McGinley, D. L. Birkenheuer, and J. R. Smart, 1996: The Local Analysis and Prediction System (LAPS): Analyses of clouds, precipitation, and temperature. *Wea. Forecasting,* **11,** 273–287.

Bannister, R. N., 2008: A review of forecast error covariance statistics in atmospheric variational data assimilation. II: Modelling the forecast error covariance statistics. *Quart. J. Roy. Meteor. Soc.,* **134,** 1971–1996.

Barker, D. M., W. Huang, Y.-R. Guo, A. J. Bourgeois, and Q. N. Xiao, 2004: A three-dimensional variational data assimilation system for MM5: Implementation and initial results. *Mon. Wea. Rev.,* **132,** 897–914.

——, and Coauthors, 2012: The Weather Research and Forecasting (WRF) Model's Community Variational/Ensemble Data Assimilation System: WRFDA. *Bull. Amer. Meteor. Soc.,* **93,** 831–843.

Caumont, O., V. Ducrocq, É. Wattrelot, G. Jaubert, and S. Pradier-vabre, 2010: 1D+3DVar assimilation of radar reflectivity data: A proof of concept. *Tellus,* **62A,** 173–187.

Chen, M., S. Fan, J. Zhong, X.-Y. Huang, Y.-R. Guo, W. Wang, Y. Wang, and B. Kuo, 2009: A WRF-based rapid updating cycling forecast system of BMB and its performance during the summer and Olympic Games 2008. *Proc. WMO Symp. on Nowcasting,* Whistler, BC, Canada, WMO, 6 pp. [Available online at http://www.mmm.ucar.edu/wrf/users/workshops/WS2009/abstracts/P3B-37.pdf.]

Courtier, P., J.-N. Thépaut, and A. Hollingsworth, 1994: A strategy for operational implementation of 4D-Var, using an incremental approach. *Quart. J. Roy. Meteor. Soc.,* **120,** 1367–1387.

Dowell, D. C., F. Zhang, L. J. Wicker, C. Snyder, and N. A. Crook, 2004: Wind and temperature retrievals in the 17 May 1981 Arcadia, Oklahoma, supercell: Ensemble Kalman filter experiments. *Mon. Wea. Rev.,* **132,** 1982–2005.

——, L. J. Wicker, and C. Snyder, 2011: Ensemble Kalman filter assimilation of radar observations of the 8 May 2003 Oklahoma City supercell: Influences of reflectivity observations on storm-scale analyses. *Mon. Wea. Rev.,* **139,** 272–294.

Fan, S.-Y., C. Zhang, and J. Zhong, 2006: Contrast analysis of background error of MM5 3DVAR system in cloud and warm season in Beijing. *Plateau Meteor.,* **25,** 855–861.

——, and Coauthors, 2008: Application of WRF 3DVar to a high resolution model over Beijing area. *Plateau Meteor.,* **27,** 1181–1188.

Gao, J., and D. J. Stensrud, 2012: Assimilation of reflectivity data in a convective-scale, cycled 3DVAR framework with hydrometeor classification. *J. Atmos. Sci.,* **69,** 1054–1065.

——, M. Xue, K. Brewster, and K. K. Droegemeier, 2004: A three-dimensional variational data assimilation method with recursive filter for single-Doppler radar. *J. Atmos. Oceanic Technol.,* **21,** 457–469.

Honda, Y., M. Nishijima, K. Koizumi, Y. Ohta, K. Tamiya, T. Kawabata, and T. Tsuyuki, 2005: A pre-operational variational data assimilation system for a non-hydrostatic model at the Japan Meteorological Agency: Formulation and preliminary results. *Quart. J. Roy. Meteor. Soc.,* **131,** 3465–3475.

Hu, M., M. Xue, and K. Brewster, 2006: 3DVAR and cloud analysis with WSR-88D level-II data for the prediction of the Fort Worth, Texas, tornadic thunderstorms. Part I: Cloud analysis and its impact. *Mon. Wea. Rev.,* **134,** 675–698.

Jung, Y., M. Xue, G. Zhang, and J. M. Straka, 2008: Assimilation of simulated polarimetric radar data for a convective storm using the ensemble Kalman filter. Part II: Impact of polarimetric data on storm analysis. *Mon. Wea. Rev.,* **136,** 2246–2260.

Lim, E., and J. Sun, 2010: A four-dimensional velocity dealiasing technique using rapidly updated analysis in a variational Doppler radar data assimilation system. *J. Atmos. Oceanic Technol.,* **27,** 1140–1152.

Lim, S., V. Chandrasekar, and V. N. Bringi, 2005: Hydrometeor classification system using dual-polarization radar measurements: Model improvements and in situ verification. *IEEE Trans. Geosci. Remote Sens.,* **43,** 792–801.

Marzano, F. S., D. Scaranari, M. Celano, P. P. Alberoni, G. Vulpiani, and M. Montopoli, 2006: Hydrometeor classification from dual-polarized weather radar: Extending fuzzy logic from S-band to C-band data. *Adv. Geosci.,* **7,** 109–114.

Michelson, S. A., and N. L. Seaman, 2000: Assimilation of NEXRAD-VAD winds in summertime meteorological simulations over the northeastern United States. *J. Appl. Meteor.,* **39,** 367–383.

Parrish, D., and J. Derber, 1992: The National Meteorological Center's spectral statistical interpolation analysis system. *Mon. Wea. Rev.,* **120,** 1747–1763.

Roberts, N. M., and H. W. Lean, 2008: Scale-selective verification of rainfall accumulations from high-resolution forecasts of convective events. *Mon. Wea. Rev.,* **136,** 78–97.

Skamarock, W. C., and Coauthors, 2008: A description of the advanced research WRF version 3. NCAR Tech. Note TN-475+STR, 113 pp.

Souto, M. J., C. F. Balseiro, V. Pérez-Muñuzuri, M. Xue, and K. Brewster, 2003: Impact of cloud analysis on numerical weather prediction in the Galician region of Spain. *J. Appl. Meteor.,* **42,** 129–140.

Sugimoto, S., N. A. Crook, J. Sun, Q. Xiao, and D. M. Barker, 2009: An examination of WRF 3DVAR radar data assimilation on its capability in retrieving unobserved variables and forecasting precipitation through observing system simulation experiments. *Mon. Wea. Rev.,* **137,** 4011–4029.

Sun, J., 2005a: Convective-scale assimilation of radar data: Progress and challenges. *Quart. J. Roy. Meteor. Soc.,* **131,** 3439–3463.

——, 2005b: Initialization and numerical forecasting of a supercell storm observed during STEPS. *Mon. Wea. Rev.,* **133,** 793–813.

——, and N. A. Crook, 1997: Dynamical and microphysical retrieval from Doppler radar observations using a cloud model and its adjoint. Part I: Model development and simulated data experiments. *J. Atmos. Sci.,* **54,** 1642–1661.

Sun, J.-H., X.-L. Zhang, J. Wei, and S.-X. Zhao, 2005: A study on severe heavy rainfall in north China during the 1990s (in Chinese). *Climatic Environ. Res.,* **10,** 492–506.

Tong, M., and M. Xue, 2005: Ensemble Kalman filter assimilation of Doppler radar data with a compressible nonhydrostatic model: OSS experiments. *Mon. Wea. Rev.,* **133,** 1789–1807.

——, and ——, 2008: Simultaneous estimation of microphysical parameters and atmospheric state with simulated radar data and ensemble square-root Kalman filter. Part II: Parameter estimation experiments. *Mon. Wea. Rev.,* **136,** 1649–1668.

Wang, H., J. Sun, Y.-R. Guo, X.-Y. Huang, and S. Sugimoto, 2011: Radar reflectivity data assimilation with the four-dimensional variational system of the Weather Research and Forecast model. Preprints, *15th Symp. on Integrated Observing and Assimilation Systems for the Atmosphere, Oceans and Land Surface,* Seattle, WA, Amer. Meteor. Soc., J17.4. [Available online at https://ams.confex.com/ams/91Annual/webprogram/Paper185272.html.]

Weygandt, S. S., S. G. Benjamin, T. G. Smirnova, and J. M. Brown, 2008: Assimilation of radar reflectivity data using a diabatic digital filter within the Rapid Update Cycle. Preprints, *12th Conf. on IOAS-AOLS,* New Orleans, LA, Amer. Meteor. Soc., 8.4. [Available online at https://ams.confex.com/ams/88Annual/webprogram/Paper134081.html.]

Xiao, Q., and J. Sun, 2007: Multiple-radar data assimilation and short-range quantitative precipitation forecasting of a squall line observed during IHOP_2002. *Mon. Wea. Rev.,* **135,** 3381–3404.

——, Y. Kuo, J. Sun, W. Lee, E. Lim, Y.-R. Guo, and D. M. Barker, 2005: Assimilation of Doppler radar observations with a regional 3DVAR system: Impact of Doppler velocities on forecasts of a heavy rainfall case. *J. Appl. Meteor.,* **44,** 768–788.

——, ——, ——, ——, D. M. Barker, and E. Lim, 2007: An approach of Doppler reflectivity data assimilation and its assessment with the inland QPF of Typhoon Rusa (2002) at landfall. *J. Appl. Meteor. Climatol.,* **46,** 14–22.

Xue, M., M. Tong, and K. K. Droegemeier, 2006: An OSSE framework based on the ensemble square-root Kalman filter for evaluating impact of data from radar networks on thunderstorm analysis and forecast. *J. Atmos. Oceanic Technol.,* **23,** 46–66.

Yang, Y., C. Qiu, and J. Gong, 2006: Physical initialization applied in WRF-Var for assimilation of Doppler radar data. *Geophys. Res. Lett.,* **33,** L22807, doi:10.1029/2006GL027656.

Zhang, J., F. Carr, and K. Brewster, 1998: ADAS cloud analysis. Preprints, *12th Conf. on Numerical Weather Prediction,* Phoenix, AZ, Amer. Meteor. Soc., 185–188.

Zhao, Q., and Y. Jin, 2008: High-resolution radar data assimilation for Hurricane Isabel (2003) at landfall. *Bull. Amer. Meteor. Soc.,* **89,** 1355–1372.